Mechanistic Insight into the Effect of Cu Doping on Thermoelectric Properties of Sintered Wet-Chemically Synthesised $SnSe_2$ Nanosheets

Simon Moore,[1] Mari Takahashi,[1] Philipp Sauerschnig,[2] Keiji Kobayashi,[1] Koichi Higashimine,[3]

Masanobu Miyata,[1] Takahiro Baba,[4,5] Jun Uzuhashi,[6] Michihiro Ohta,[2] Takao Mori,[4,5]

*Tadakatsu Ohkubo,[6] Shinya Maenosono[1]**

[1] School of Materials Science, Japan Advanced Institute of Science and Technology, 1-1 Asahidai, Nomi, Ishikawa 923-1292, Japan

[2] Global Zero Emission Research Center, National Institute of Advanced Industrial Science and Technology (AIST), Tsukuba, Ibaraki 305-8569, Japan

[3] Center for Nano Materials and Technology, Japan Advanced Institute of Science and Technology, 1-1 Asahidai, Nomi, Ishikawa 923-1292, Japan

[4] Research Center for Materials Nanoarchitectronics, National Institute for Materials Science (NIMS), 1-1 Namiki, Tsukuba, Ibaraki 305-0044, Japan

[5] Graduate School of Pure and Applied Science, University of Tsukuba, Tennoudai 1-1-1, Tsukuba, Ibaraki 305-8671, Japan

[6] Research Center for Magnetic and Spintronic Materials, National Institute for Materials Science (NIMS), 1-2-1 Sengen, Tsukuba, Ibaraki 305-0047, Japan

Corresponding Author*

Email: shinya@jaist.ac.jp

Phone: +81-761-51-1611

ABSTRACT

$SnSe_2$ – an uncommon, sustainable n-type thermoelectric material – has previously been doped with elements including Cu to improve its thermoelectric figure of merit, *ZT* value. However, the effects and mechanisms behind Cu doping remain unclear. To provide important mechanistic insight, $SnSe_2$:Cu nanosheets were synthesised, sintered, and subjected to multifaceted analysis using a variety of analytical techniques. The results suggested that intercalated Cu^+ ions contribute to the density of states of the valence band, shifting the Fermi energy towards the conduction band. The carrier concentration was raised, causing a shift to conduction across two conduction band minima. Additionally, a change to ionised impurity scattering dominated carrier mobility meant a high mobility at high temperatures, since electron-phonon interactions were insignificant. The result was a significantly increased electrical conductivity, while the thermal conductivity decreased due to scattering at nanosheet grain boundaries and Cu^+ ions. High *ZT* values of 0.2 in the in-plane, and 0.6 in the out-of-plane directions were achieved at 667 K.

Keywords: *waste heat harvesting, sustainable materials, XAFS, nanoparticles, chalcogenide*

INTRODUCTION

Converting directly between temperature differences and electrical energy via the Seebeck and Peltier effects, thermoelectric (TE) materials have garnered much attention, with a variety of semiconductors investigated for applications in waste heat harvesting,[1,2] energy generation,[3,4] cooling devices,[5] and others.[6] Of these, waste heat harvesting is considered a key technology in the development of sustainable energy systems.[6,7] The conversion efficiency of TE materials is related to the dimensionless TE figure of merit, $ZT = \sigma S^2 T/\kappa$, where σ is electrical conductivity; S is the Seebeck coefficient; T is the absolute temperature; and $\kappa = \kappa_e + \kappa_l$ is the total thermal conductivity, which includes contributions from charge carriers, κ_e (the carrier thermal conductivity), and phonons, κ_l (the lattice thermal conductivity). Current successfully implemented TE devices use materials such as Bi-Te[8,9] and Pb-Te,[10,6] for which recent developments have seen high *ZT* values of 1.24 at 350 K for $Bi_{0.5}Sb_{1.5}Te_3$ – 20wt% Te[11] and 2.8 at 850 K for $Na_{0.03}Pb_{0.97}Te$ – 2% MgTe – 0.75% GeTe.[12] However, the use of rare or highly toxic elements such as Te, Sb and Pb means that such materials are considered unsustainable for future, large-scale, practical use.[13] On the other hand, more sustainable materials, such as copper tin sulphide[14] and metal chalcogenides other than tellurides,[15,16] have lower intrinsic *ZT* values, so research has focused on their improvement. The path to higher *ZT* lies in increasing the power factor ($PF = \sigma S^2$), while simultaneously decreasing κ. The methods to do so include dopant atoms to increase σ;[17,18] band engineering to maximise *PF*;[19,20] and defect engineering (for example, the introduction of controlled nanograin boundaries), which decreases κ through increased phonon scattering.[21,22]

One highly discussed sustainable TE material is tin monoselenide (SnSe), a p-type semiconductor with a layered, orthorhombic crystal structure (Figure S1a). Made of relatively abundant elements with low toxicity (further discussion of the sustainability of Sn-Se can be found in the Supporting Information and Figure S2), it caused a stir with a reported maximum *ZT* value of 2.6 along the b-axis at 923 K for the single crystal, thanks to its anharmonic structure creating a low intrinsic κ (0.35 $W \cdot m^{-1} \cdot K^{-1}$ along the b-axis at 923 K).[23] Polycrystalline SnSe generally showed lower TE performance but recent developments have seen significant improvements,[24] with strategies such as Ge alloying resulting in a high *ZT* of 1.75 at 873 K.[25] Another strategy focused on the removal of a tin oxide layer, which often forms on the outside of SnSe grains thanks to the exposed Sn atoms and thus has a detrimental effect on the TE performance of polycrystalline SnSe. Removal of this layer by a reducing gas led to a reported maximum *ZT* of 3.1 at 783 K.[26] Although intrinsically a p-type semiconductor, doping to create n-type SnSe has also borne fruit with high *ZT* values reported,[27,28] including a value of 2.23 at 873 K for Cd and Pb-doped SnSe,[29] which represents a record high for all reported n-type polycrystalline materials.

In contrast, the n-type, hexagonal, Van der Waals (VdW) structured (Figure S1b) tin diselenide ($SnSe_2$) has a much lower *ZT* value, (0.10 and 0.15 at 673 K along the ab-plane and c-axis, respectively) due to its rigid hexagonal crystal structure giving a high intrinsic κ, and a relatively low carrier concentration (approximately 2.3×10^{18} cm^{-3} at 300 K) resulting in low *PF*s of 3.5 and 1.0 $\mu W \cdot cm^{-1} \cdot K^{-2}$ at 673 K for the ab-plane and c-axis, respectively.[30] However, $SnSe_2$ has shown promise as a sustainable n-type TE material, with significant increases in *PF* and *ZT* reported for Cl and Br doping, which substitute in Se sites and increase the carrier concentration. High *ZT* values were reported of 0.3 (in-plane, perpendicular to the pressing direction) and 0.4 (out-of-plane, parallel to the pressing direction) at 673 K for 12% Cl-doping;[31] and 0.25 (in-plane) and

0.55 (out-of-plane) at 670 K for 10% Br-doping.[32] Interestingly, although n-type SnSe has demonstrated very high *ZT* values in the higher temperature ranges ($>$ 600 K), the reports of halogen-doped n-type $SnSe_2$ have shown improved *ZT* values at more moderate temperatures (between 400 and 600 K). Given that the value of κ remains high and σ remains low for these materials suggests that with further improvement, $SnSe_2$ holds potential as a TE material for this temperature range. Additionally, thanks to the complete surrounding of Sn atoms by Se in the crystal structure of $SnSe_2$ (Figure S1b), it does not suffer from the surface oxidation problem of polycrystalline SnSe, simplifying the fabrication process.

As another way to improve the electrical properties of $SnSe_2$, small amounts of Cu doping have also been trialled. Wang *et al*. reported a remarkably high *ZT* of 0.75 at 300 K for polycrystalline $SnCu_{0.01}Se_2$.[33] Although, they did not account for the anisotropy in the TE properties, so the practical *ZT* value is likely to be much lower. Zhou *et al*. reported an ab-plane *ZT* of approximately 0.35 at 770 K for $SnCu_{0.005}Se_2$. They also co-doped Cu with Br to achieve a maximum ab-plane *ZT* of 0.6 at 770 K for $SnCu_{0.005}Se_{1.98}Br_{0.02}$.[34] While both reports demonstrated that Cu could be an effective dopant, their contrasting results also suggested that different mechanisms were in play. For Wang *et al*., Cu doping increased the Hall carrier concentration, n_H, and decreased Hall mobility, μ_H, across the measured temperature range (10–300 K). On the other hand, Zhou *et al*.'s $SnCu_{0.005}Se_2$ showed no change in n_H until the temperature exceeded 600 K. Based on atom probe tomography, scanning transmission electron microscopy (STEM) and density functional theory (DFT) calculations, they concluded that Cu atoms intercalated in the VdW gap of $SnSe_2$, and that their ionization at high temperatures increased n_H. Bridging of the VdW gap by Cu atoms and electron delocalisation in the surrounding Se atoms also enhanced μ_H. In contrast, Wang *et al*. did not investigate Cu's position in the crystal lattice nor the mechanism of electron donation.

Additionally, other reports have included Cu as a co-dopant alongside Br,[35] with one report combining this with heat treatment of the sample to produce a high *ZT* of approximately 1.1 at 770 K.[36] However, these reports did not focus on investigating the effects of the Cu doping itself. As a result, the exact mechanism of Cu doping in $SnSe_2$ remains unclear and we are unable to reconcile or reproduce the contrasting results of Wang *et al*. and Zhou *et al*.

Cu is also a popular dopant in other n-type and p-type TE materials, such as SnSe,[37] ZnSb,[38] Bi_2Te_3,[39] and $Bi_2Te_{2.7}Se_{0.3}$.[40] Cu often increases n_H, and thus seems to be able to act as both an electron and hole donor, depending on the material. However, the complex mechanisms are either not fully clear or not investigated in detail, especially for nanostructured materials and $SnSe_2$.

To provide a mechanistic insight into Cu doping of $SnSe_2$ and, by extension, other n-type TE materials, we present a thorough investigation into the TE properties of Cu-doped $SnSe_2$ nanosheets (NSs), synthesised based on our previous report,[41] while Cu doping was achieved through a Cu impurity in the Sn precursor. The NSs were sintered into pellets by hot press, after which the TE properties and the electronic transport properties were investigated by light flash analysis (LFA), ZEM-3, and a physical properties measurement system (PPMS). A thorough structural analysis was performed by X-ray diffraction (XRD), scanning transmission electron microscopy (STEM), scanning electron microscopy (SEM), energy dispersive x-ray spectroscopy (EDS), X-ray photoelectron spectroscopy (XPS), and three-dimensional atom probe (3DAP). X-ray absorption fine structure (XAFS) Sn and Se K-edge measurements and DFT calculations helped investigate the mechanism in more detail. High *ZT*s of approximately 0.2 in the in-plane (IP) direction, and 0.6 in the out-of-plane (OOP) direction at 667 K were observed – among the highest values reported for $SnSe_2$.[17,30-36,42] The characterisation and analysis provide new insights into the mechanisms of Cu doping in $SnSe_2$, which help to explain the observed properties.

EXPERIMENTAL SECTION

Chemicals

Oleylamine (OLA, technical grade 70%), tin (IV) acetate ($Sn(OAc)_4$), selenium powder (Se, 100 mesh, purity 99.99% metals basis), trioctylphosphine oxide (TOPO, technical grade 90%), and tin (IV) fluoride (SnF_4) were purchased from Sigma Aldrich. Thiourea (purity > 99.0%) was purchased from Tokyo Chemical Industry Co. Ltd. Toluene was purchased from Fujifilm Wako and methanol was purchased from Kanto Chemical. All chemicals were used without further modification.

Synthesis of $SnSe_2$:Cu and $SnSe_2$ NSs

$SnSe_2$ NSs were synthesised using the method in our previous report[41] with the following changes. The scale was increased to use five times the reported amounts and the ratio of the Sn to Se precursors was set at 1:10 to produce pure phase $SnSe_2$ NSs. $SnSe_2$ NSs without the Cu impurity were synthesised by changing the Sn precursor to SnF_4, which was included in the flask from the start of the synthesis instead of being injected. The total amount of OLA, TOPO, and Se, as well as the temperature profile were kept identical.

Ligand exchange

Approximately 1.20 g of as-synthesised $SnSe_2$ NSs were dispersed in 18.75 mL of toluene in a conical beaker by sonication. At the same time, 3.75 g of thiourea was dissolved in 56.25 mL of methanol. After the NSs were completely dispersed and the thiourea completely dissolved, the thiourea-methanol solution was added to the NS-toluene mix and the two sonicated together for two hours, with occasional swilling by hand. Then, the mixture was separated into four 50 mL centrifuge tubes and centrifuged at 4,640 × *g* for 5 mins, after which the supernatant was discarded. After this, washing was performed by redispersing the NSs using 22.5 mL of methanol in each

tube, followed by centrifugation at 4,640 × *g* for 5 mins and the disposal of the supernatant. This washing step was performed four times, and the final product was dried in a vacuum. Thermogravimetric analysis (TGA, TGA/SDTA851, Mettler Toledo) was used to confirm the success of the ligand exchange.

Pelletisation

After ligand exchange, the NS powder was sintered into a pellet using a hot press at a pressure of 300 MPa for 30 mins at 400 °C in an Ar atmosphere. In total, three 10 mm diameter cylindrical pellets were produced – two that were 2 mm thick and one that was 8 mm thick.

Characterisation

As synthesised NSs were characterised as shown in our previous report.[41] After ligand exchange the NSs were characterised using powder X-ray diffraction (XRD, Mini-Flex600, Rigaku) using a Cu Kα source; scanning electron microscopy equipped with energy dispersive X-ray spectroscopy (SEM-EDS, Miniscope TM3030Plus, Hitachi) at an acceleration voltage of 15 kV; transmission electron microscopy (TEM, H-7650, Hitachi) at an acceleration voltage of 100 kV; scanning TEM (STEM, JEM-ARM200F, JEOL) at an acceleration voltage of 200 kV, equipped with EDS and a high-angle annular dark field detector (HAADF); and X-ray photoelectron spectroscopy (XPS, AXIS-ULTRA DLD, Shimadzu/Kratos) using a monochromated Al Kα source.

X-ray absorption fine structure (XAFS) analysis was performed by measuring the Sn and Se K-edge X-ray absorption near edge structure (XANES) and extended X-ray absorption fine structure (EXAFS) in transmission mode at the NW-10A beamline of the Photon Factory – Advanced Ring (PF-AR) facility at the High Energy Accelerator Research Organisation (KEK) in Tsukuba, Japan. The energy and current of the electrons in the storage ring were 6.5 GeV and 60 mA, respectively.

After sintering, the pellets were first polished using silicon carbide abrasive paper (grit size 2,000) and then had their densities measured using a gas pycnometer (Shimadzu AccuPyc II 1340) and by calculation based on the measured mass and dimensions of each pellet. Powders of the pellets were characterised by XRD, SEM-EDS and XPS. The pellets' outer surfaces were also characterised by SEM-EDS. For further investigation an offcut from one of the 2 mm pellets had its cross-section investigated. It was first polished using an Ar beam polisher (IM4000, Hitachi High-Tech), followed by observation by SEM-EDS (CrossBeam550, CarlZeiss) at an acceleration voltage of 15 kV. Following this a small, thin rectangular sheet and a small cone were cut from the cross section of the pellet, as shown in Figure S3, using an FIB-SEM dual beam system (Helios 5UX, Thermo Fisher Scientific). The rectangular sheet was further thinned and mounted onto a sample holder for observation by STEM (Titan G2 80-200, Thermo Fisher Scientific) equipped with HAADF and EDS. The cone was then used for measurement by 3D atom probe (3DAP, LEAP 5000XS, CAMECA) using a 355 nm wavelength laser pulsing mode at a repetition rate of 250 kHz and a laser energy of 20 pJ with the sample temperature set to 30 K.

TE properties measurement

Each pellet had its density measured using a gas pycnometer (Shimadzu Accupyc II 1340 pycnometer) in a He atmosphere. The thermal diffusivity, D ($m^2 \cdot s^{-1}$) was measured using light flash analysis (LFA, Netzsch LFA467). The specific heat, c ($J \cdot kg^{-1} \cdot K^{-1}$), was derived by measuring the sample and a standard sample (Pyroceram 9606, Netsch) under the same conditions using the same LFA. κ was then calculated from the relationship $\kappa = dcD$, where d is density ($kg \cdot m^{-3}$). Electrical properties (σ and S) were measured using a ZEM-3 instrument (Advance Riko) for a temperature range of 350–667 K. PF and ZT were calculated using $PF = \sigma S^2$ and $ZT = (\sigma S^2/\kappa)T$. The carrier thermal conductivity, κ_e was calculated from the Wiedermann-Franz

Law $\kappa_e = L\sigma T$ where L is the Lorentz number (2.44×10^{-8} W·Ω·K^{-2}) and κ_l was calculated by $\kappa_l = \kappa - \kappa_e$. The pellet preparation and measurement technique are shown in Figure S4. One of the 2 mm thick pellets had its out-of-plane (OOP, parallel to the pressing direction) κ measured by LFA, before it was cut into a rectangular bar and the in-plane (IP, perpendicular to the pressing direction) σ and S were measured by ZEM-3. The 8 mm thick pellet was first sanded down into a 6 mm × 8 mm × 2 mm pellet in which the 6 mm side was parallel to the pressing direction. The IP κ and OOP σ and S were then measured in the same manner as the first pellet.

The error bars for the TE properties were calculated using known measurement errors of 5% for the values measured by ZEM-3 (σ and S), and 7% for κ measured by LFA. Based on these, the maximum and minimum possible values of σ, S, and κ were calculated, these were then used to calculate the maximum and minimum possible values of PF and ZT.

To investigate the possibility of measuring κ in the IP direction using a thin pellet, the second 2 mm thick pellet first had its OOP D measured by LFA (Netzsch LFA467) (Figure S5a). The pellet was then cut into a rectangular bar, and the same LFA device was used to heat the bar at both ends while the thermal response was measured in the middle. A COMSOL simulation was then used in which the OOP D was fixed by the previous measurement and the IP D was varied until it matched the measured signal (Figure S5b). Then IP κ was calculated from the equation $\kappa = dcD$.

Electronic transport properties measurement

After measurement of the TE properties by LFA and ZEM-3, n_H, μ_H, and temperature dependence of the electrical resistivity, ρ, were measured using a Physical Properties Measurement System (PPMS, Quantum Design). For the measurement, gold wire electrodes were attached to the pellet using a gold paste. A thin layer of gold was applied via sputtering to the locations which would be used for the electrodes to enhance adhesion and reduce contact resistance.

The pellet was placed on a copper plate and then onto the sample puck, at which point the gold wires were connected to the terminals of the sample puck using a silver paste. The Hall voltage, V_{H} was measured over a temperature range of 10–340 K, under a magnetic field of ± 5 T and a current of 30 mA. ρ was measured over a temperature range of 3–340 K at a heating rate of 1 K·min^{-1}, under a current of 30 mA. The Hall coefficient, R_{H}, was calculated using $R_{\mathrm{H}} = V_{\mathrm{H}}t/BI$ where t is the thickness of the pellet (m), B is the magnetic field (T), and I is the applied current (A). n_{H} was then calculated using $n_{\mathrm{H}} = 1/eR_{\mathrm{H}}$ where e is the elementary charge, and μ_{H} was found using $\mu_{\mathrm{H}} = 1/e\rho n_{\mathrm{H}}$.

The weighted mobility, μ_{W}, was calculated using the values for S and σ measured by ZEM-3 and the following equation:[43]

$$\mu_{\mathrm{W}} = \frac{3h^2\sigma}{8\pi e(2m_e k_{\mathrm{B}}T)^{3/2}}\left[\frac{\exp\left[\frac{|S|}{k_{\mathrm{B}}/e}-2\right]}{1+\exp\left[-5\left(\frac{|S|}{k_{\mathrm{B}}/e}\right)-1\right]}+\frac{\frac{3}{\pi^2}\frac{|S|}{k_{\mathrm{B}}/e}}{1+\exp\left[5\left(\frac{|S|}{k_{\mathrm{B}}/e}\right)-1\right]}\right] \qquad \text{(Eqn. 1)}$$

where h is the Planck constant, e is the elementary charge, m_e is the electron rest mass, k_{B} is the Boltzmann constant, and $|S|$ is the magnitude of the Seebeck coefficient (V·K^{-1}).

Density functional theory calculations

The electronic structure of an $SnSe_2$(*P-3m1*) primitive cell and a Cu intercalated $SnSe_2$ supercell, which included eight Sn, sixteen Se, and a Cu atom, were calculated using the OpenMX software package[44,45] based on density-functional theory (DFT), norm-conserving pseudopotentials, and pseudo-atomic localized basis functions. We applied the generalized gradient approximation proposed by Perdew, Burke, and Ernzerhof.[46] The contribution of spin-orbit coupling was also considered. The pseudo-atomic orbital basis functions are specified as Se7.0-s3p2d1, Sn7.0-

s3p2d1 and Cu6.0S-s2p1d1, where the symbols respectively denote the element, cutoff radius (Bohr), and specification of the optimized orbitals. We applied the unit cell with *k*-point grids (*k* grids) of $14\times14\times8$ and $7\times7\times4$ for the $SnSe_2$ cell and the Cu intercalated $SnSe_2$ supercell. We set an energy cutoff of 220 Ry for numerical integration. We performed an optimization of the lattice constants and atomic positions using the steepest descent method, with a force criterion of less than 2.0×10^{-4} Hartree $Bohr^{-1}$.

RESULTS AND DISCUSSION

Structural characterisation of Cu-doped $SnSe_2$ nanosheets and pellets

Cu-doped, pure-phase, hexagonal $SnSe_2$ NSs ($SnSe_2$:Cu) were synthesised using a scaled-up version of our previously reported method.[41] XRD and TEM of the produced NSs are shown in Figure S6. The Cu impurity was initially discovered by SEM-EDS and STEM-EDS (Figure S7) of the NSs and confirmed by XPS analysis of the pellet with a detected amount of 1.2 at% relative to Sn. The Cu 2p and Cu $L_3M_{4,5}M_{4,5}$ Auger regions of the XPS spectra are show in Figure S8. The Sn precursor, $Sn(OAc)_4$, was the source of the Cu impurity, with SEM-EDS and XPS analysis suggesting a composition of approximately 2.4 at% Cu (Figure S9 and Table S1). Multiple syntheses with different bottles produced the same results, suggesting that Cu is always present, though the manufacturing process of $Sn(OAc)_4$ has not been made public. The weak XPS signal for the Cu $L_3M_{4,5}M_{4,5}$ Auger region made full deconvolution difficult, but the Cu 2p peaks' binding energies suggested the presence of Cu^+ in the $SnSe_2$:Cu pellet and Cu metal in $Sn(OAc)_4$, indicating oxidation taking place during the synthesis.

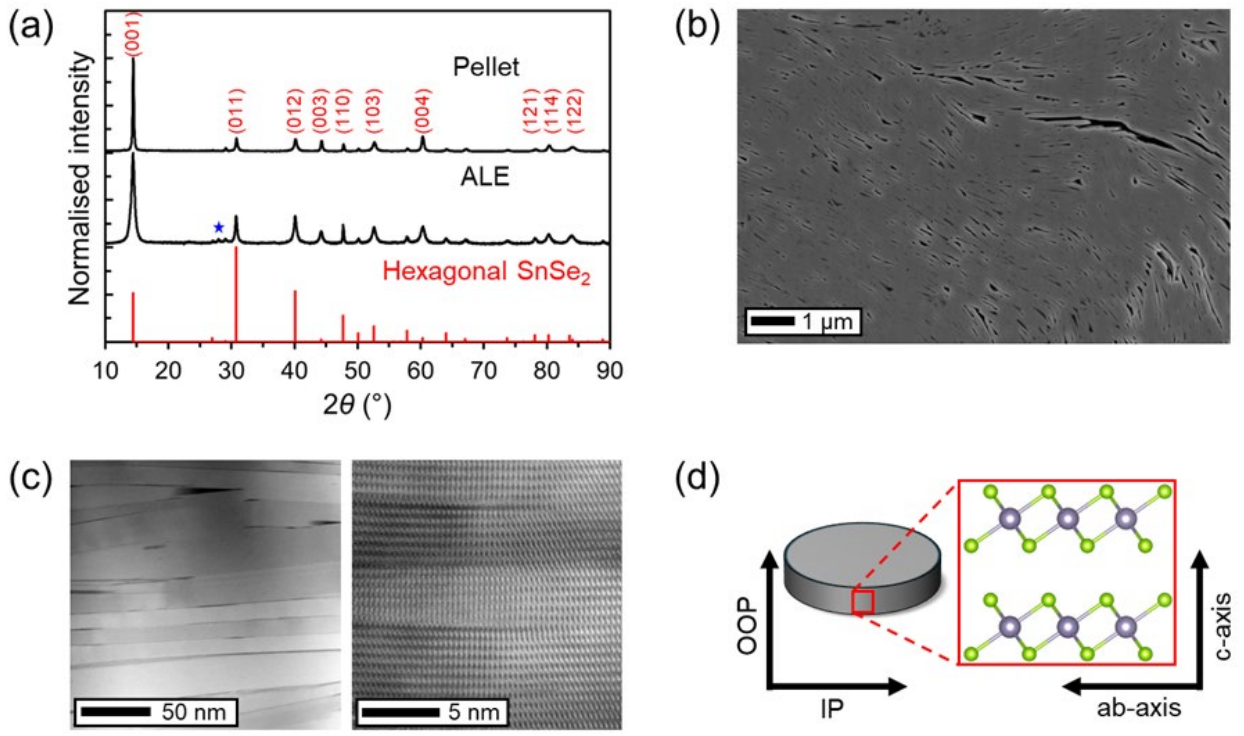

Figure 1. Characterisation of the $SnSe_2$:Cu pellets. (a) XRD pattern with after ligand exchange (ALE) NSs as a comparison. Red is reference pattern for hexagonal $SnSe_2$ (PDF: 01-089-2939). The blue star is a peak originating from a damaged XRD substrate. (b) SEM and (c) STEM-HAADF images showing the arrangement of NSs in the pellet. In the SEM and STEM images, the vertical direction is the OOP direction. (d) Schematic image of the pellet showing how the IP and OOP directions relate to the ab-plane and c-axis of $SnSe_2$.

Since large ligands can influence the TE properties,[47] a ligand exchange was performed from trioctylphosphine oxide (TOPO) and oleylamine (OLA) to thiourea before sintering by hot press. Investigation by thermogravimetric analysis (TGA) before (BLE) and after (ALE) the ligand exchange (Figure S10), confirmed the successful exchange. Powder XRD patterns of ALE NSs and the pellet are shown in Figure 1a. All peaks except for one (at approximately 28°) could be indexed to hexagonal $SnSe_2$, though only the main peaks have been labelled in the figure. The remaining small peak at approximately 28° was found to originate from a damaged Silicon XRD substrate, the XRD pattern for which can be found in Figure S11. Mean crystalline sizes (D_{XRD})

of the (001) and (110) peaks, representing the c-axis and ab-plane, respectively, were calculated by Scherrer formula, producing 13.7 nm and 35.2 nm for the (001) and (110) peaks of the ALE NSs, and 33.7 nm and 43.5 nm for the (001) and (110) peaks of the pellet. Thus, we can see that the pellet retains the NSs' pure-phase $SnSe_2$, though some grain growth has taken place.

Cross-sectional SEM and STEM-HAADF images of the pellet are shown in Figures 1b,c and additional images can be found in Figure S12. Note that in all such images the vertical and horizontal directions represent the OOP and IP directions of the pellet, respectively. We know from our previous work on the synthesis of these $SnSe_2$:Cu NSs that the layers of the $SnSe_2$ crystal structure lie parallel to the top and bottom surface of each NS,[41] and the clearly visible atomic structure in Figure 1c confirms this to be the case in the pellet as well. From Figures 1b,c and S12, we can see that the general alignment of the NSs appears to be along the IP direction of the pellet, an observation supported by the larger grain growth evident in the (001) direction. This would suggest that the pellets' IP and OOP directions can represent the ab-plane and c-axis of $SnSe_2$, respectively (Figure 1d). However, there are a significant number of NSs with different orientations, so we can expect that, while there will be some anisotropy in the TE properties of the pellet, the anisotropy will not be as strong as that found in a single crystal. For this reason, we will continue to refer to the pellet's IP and OOP directions rather than the lattice directions of $SnSe_2$.

The voids visible in Figures 1b and S12 raise questions about the possibility of a low density or high porosity of the pellets leading to an effect on the measured TE properties. Therefore, the densities of all three pellets were determined using a gas pycnometer and the measured mass and dimensions of each pellet. With the density of single-crystal $SnSe_2$ reported to be 5.54 $g \cdot cm^{-3}$,[48] the relative densities of the three pellets were found to be 98.3%, 92.6%, and 95.6% for the two 2 mm thick pellets and the one 8 mm thick pellet, respectively. Since a minimum value of 95% is

generally considered desirable, as above this value any effects of porosity should be low, we can see that two of our pellets meet this requirement. The lower density pellet was only used for the determination of the IP κ by COMSOL simulation, the results of which – as we will see later – agreed well with the other pellets. So, we concluded that the lower density would not have a significant effect on the conclusions drawn in the rest of this paper.

The distribution of Cu was investigated using STEM-EDS (Figure S12), SEM-EDS (Figure S13), and 3DAP (Figure 2a), the results of which are summarized in the schematic diagram in Figure 2b. Segregated nanoscale Cu-rich domains were visible, with the region in the 3D atom maps having a composition of 42.41 at% Sn, 56.12 at% Se, and 1.47 at% Cu, compared to 33.36 at% Sn, 66.63 at% Se, and 0.01 at% Cu in the surrounding material. Note that 3DAP's accuracy is known to be high enough for the at% to be stated to two decimal places.[49] The nanoscale Cu-rich regions were also visible in the STEM-EDS mapping conducted on the pellet cross-section (Figure S12), although their small size makes them undetectable on the cross-sectional SEM-EDS mapping in Figure S13b. From the STEM-EDS images the volume fraction of these nanoscale Cu-rich regions can be calculated to be 0.18%. The low volume fraction of such regions suggests that they are unlikely to have a significant effect on the TE properties of $SnSe_2$:Cu and, as such, further discussion of their distribution and nature can be found in the Supporting Information. The remaining Cu, though low in concentration, is homogeneously distributed as Cu^+ ions, so we focused our investigations on their effect on the TE properties.

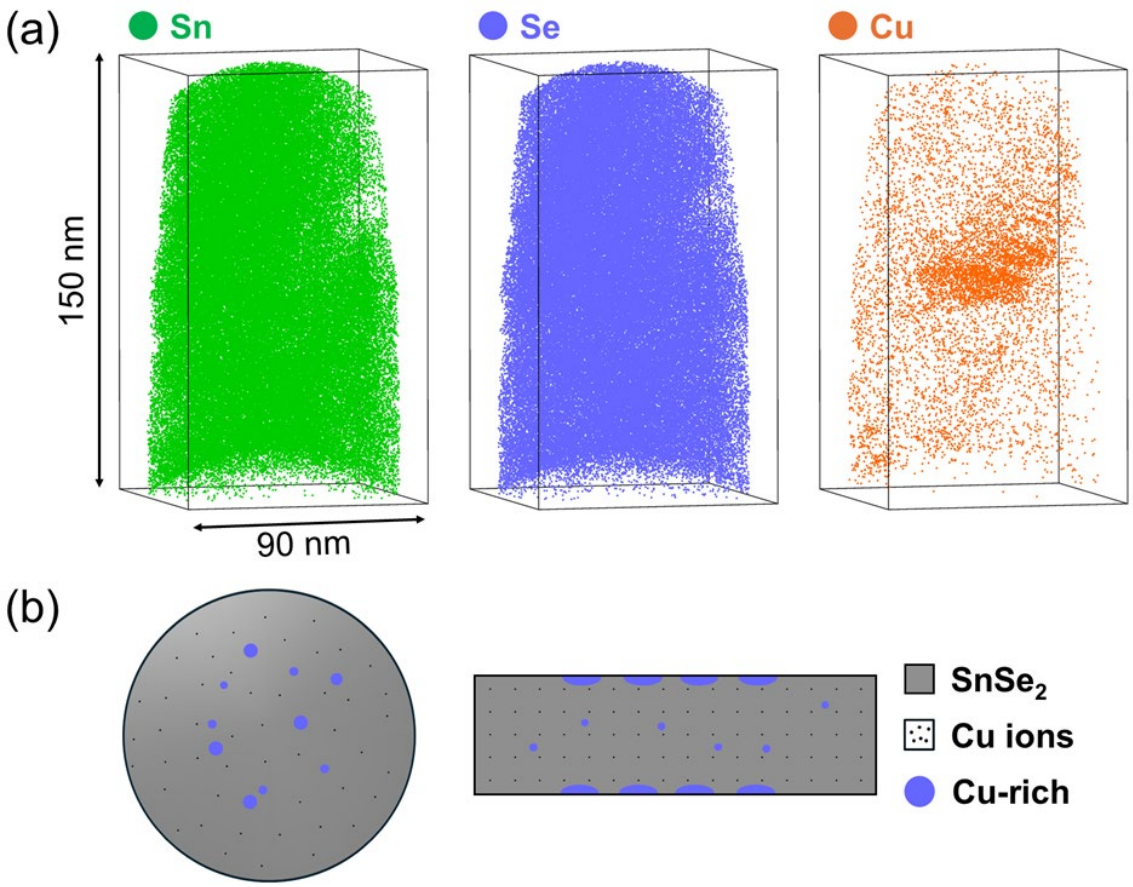

Figure 2. Characterisation of the distribution of Cu in the $SnSe_2$:Cu pellets. (a) 3D atom maps of a sample taken from the cross-section of the pellet. Green, blue, and orange represent Sn, Se, and Cu, respectively. (b) schematic image of the distribution of Cu ions (black dots) and Cu-rich regions (blue shapes) in the pellet as determined by SEM, STEM, and EDS analysis. Not to scale.

TE properties of Cu-doped $SnSe_2$

Since $SnSe_2$ has an anisotropic structure and due to the difficulty of producing thick pellets for cutting into multiple specimens, the IP and OOP direction TE properties were measured using 3 comparable pellets (Figure S4). One 2 mm thick pellet had its OOP κ measured by LFA, and IP σ and S measured using a ZEM-3. A second 2 mm thick pellet was used to estimate the IP κ at 300 K using LFA and a COMSOL simulation. An 8 mm thick pellet was cut into a plate parallel to the pressing direction for measurement of the IP κ and OOP σ and S. The results were combined to give the full IP and OOP direction TE properties of $SnSe_2$:Cu shown in Figure 3 alongside bulk,

single crystal $SnSe_2$.[30] The thermal cycling stability of the samples was confirmed by measurement over a full heating and cooling cycle for both LFA and ZEM-3, the resulting σ, S, and κ values for which are shown in full in Figure S14. The heating and cooling stages of the measurements show good agreement indicating the thermal stability of the material. It's worth noting that, as shown in the TGA results in Figure S10, $SnSe_2$ is thermally stable until approximately 550 °C (823 K), above which Se evaporation rapidly occurs. It is for this reason that the TE properties measurement temperature was limited to 393 °C (667 K).

The electrical properties of $SnSe_2$:Cu in both directions are shown in Figure 3a-c alongside those of bulk, single crystal $SnSe_2$ for comparison. An increased σ in both directions (Figure 3a), which also increased with temperature, along with a decrease in the magnitude of S (Figure 3b), suggested at an increased carrier concentration for $SnSe_2$:Cu compared with bulk $SnSe_2$. Combining these, a significantly higher *PF* in the OOP direction and a slight increase in *PF* in the IP direction (Figure 3c) was achieved. It is notable that the electrical properties in both the IP and OOP directions of $SnSe_2$:Cu are remarkably similar to each other, in contrast with the high anisotropy shown in the bulk, single crystal $SnSe_2$. As discussed earlier, and shown in Figure 1b, the anisotropy in the $SnSe_2$:Cu pellets is not as strong as that in a single crystal, which may be the reason for these results. Additionally, it should be noted that the IP and OOP direction properties were measured using different pellets, which – while they were fabricated under the same conditions – may not be completely identical, thus making some additional variation in the TE properties expected, and the comparison of the two directions difficult.

Looking at the thermal transport properties in Figures 3d,e, the IP direction κ can be clearly seen to have decreased significantly (approximately half at 350 K), while the OOP direction has only seen a slight decrease. Importantly, there was good agreement between the IP κ measured by LFA

and that estimated by our COMSOL simulation (Figure 3e), indicating that this is a valid method for the measurement of IP κ in thin pellets. We can also see that, despite the apparent increase in carrier concentration, the carrier thermal conductivity, κ_e remains extremely low to the point of being negligible, thus meaning that $\kappa = \kappa_l$ and the reductions in κ are a direct result of reduced κ_l. We have seen from Figures 1b,c that the sintering of our NSs into a single pellet has caused the creation of a large number of additional grain boundaries, which are known to reduce κ_l due to increased phonon scattering. The anisotropic crystal structure of $SnSe_2$ includes a rigid lattice extending across the ab-plane, but a layered structure including VdW gaps, which hinder the propagation of phonons, stretching along the c-axis (Figure S1). This accounts for the intrinsic high ab-plane and low c-axis κ_l of $SnSe_2$ and also the reduction we see in our nanostructured $SnSe_2$:Cu pellet. The large number of additional grain boundaries in the IP direction significantly increases phonon scattering and reduces κ_l. In the OOP direction, on the other hand, the number of additional grain boundaries, with an average spacing of about 30 nm based on the mean crystalline size, still does not compare to the number of VdW gaps that would exist along the c-axis of a single crystal, thus explaining the very slight reduction.

Overall, the *ZT* value (Figure 3f) in both directions significantly increased compared to bulk, single crystal $SnSe_2$, with maximums of 0.2 in the IP direction and 0.6 in the OOP direction at 667 K. From these results we can see that although both directions experienced an increase in *PF* and a reduction in κ, the main contributors to the increases in *ZT* were the decreased κ in the IP direction, but the increased *PF* in the OOP direction. These results compare very favourably with those of other reports,[35,36] as shown in Figure S15, where maximum *ZT* values (regardless of measurement direction) of several reports of Cu-doped $SnSe_2$ have been reproduced. We can see that only the Cu and Br co-doped and heat treated $SnSe_{1.97}Br_{0.03}$ – 3% Cu AHE (after heat

treatment) reported by Wei *et al.* showed a higher result.[36] Note that, as we mentioned previously, the notably high *ZT* at 300 K reported by Wang *et al.*[33] does not take into account the anisotropic nature of $SnSe_2$, making this value unreliable, and thus has not been included in this comparison.

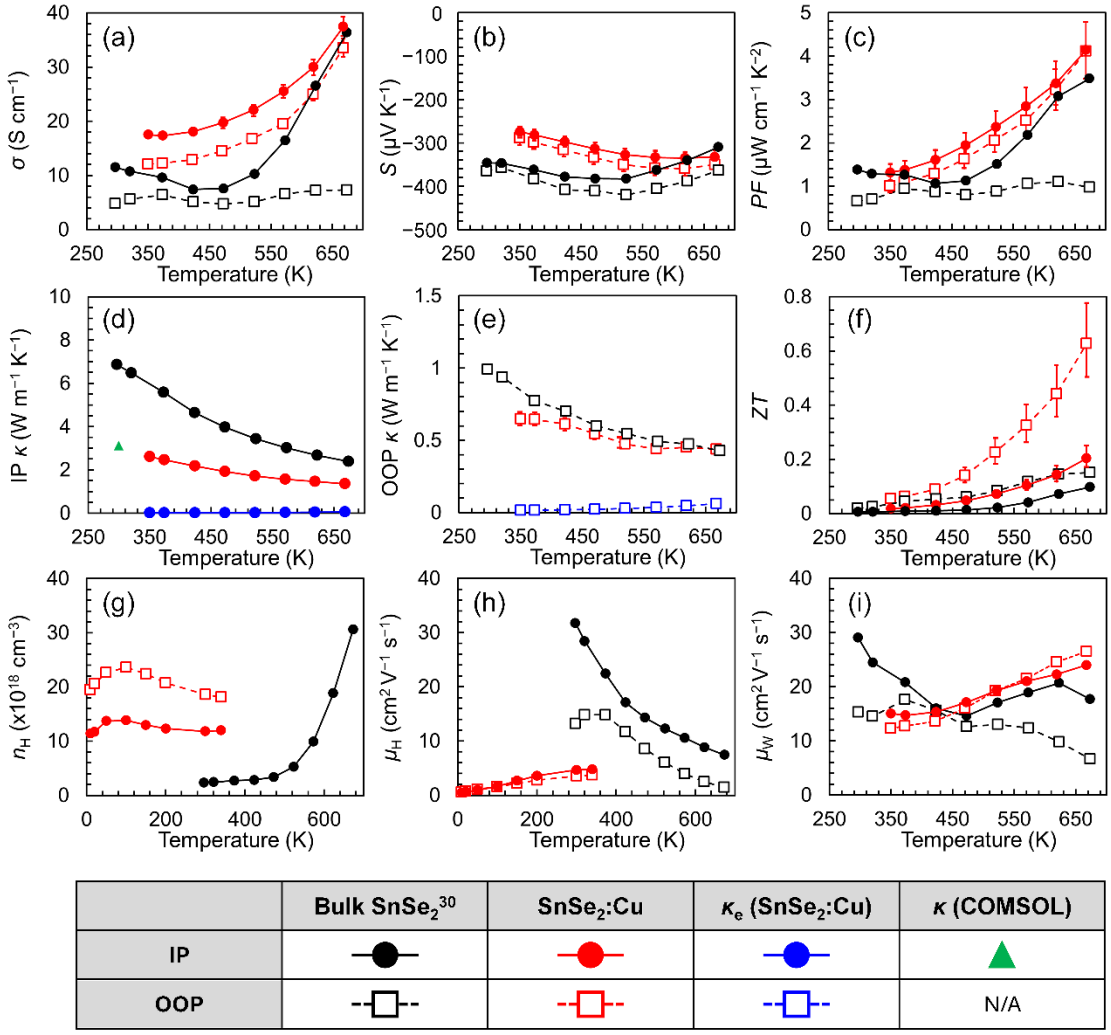

Figure 3. TE and electronic transport properties of the $SnSe_2$:Cu pellets (red) and bulk, single crystal $SnSe_2$ (black, reported in reference 30) in the IP (solid circles and lines), and OOP (open squares and dashed lines) directions. (a) electrical conductivity, σ; (b) Seebeck coefficient, S; (c) power factor, PF; (d) IP thermal conductivity; (e) OOP thermal conductivity; (f) ZT value; (g) Hall carrier concentration, n_H; (h) Hall mobility, μ_H; and (i) weighted mobility, μ_W. The carrier thermal conductivity, κ_e, is also shown in blue in (d) and (e). The green triangle in panel (e) is the value of IP κ estimated at 300 K using the COMSOL simulation.

The carrier transport properties of $SnSe_2$:Cu were investigated by PPMS, with n_H (Figure 3g) and μ_H (Figure 3h), measured between 10 and 340 K. For higher temperatures, the weighted mobility, μ_W (Figure 3i), was calculated from the σ and S measured by ZEM-3 and using Eqn. 1 in the experimental section.[43] $SnSe_2$:Cu has a higher n_H than bulk $SnSe_2$ across the measured temperature range, indicating easily-activated shallow donor levels. μ_H, on the other hand, is lower in both directions and significantly disagrees with the calculated μ_W (Figure 3h,i). The increase of carrier scattering at grain boundaries and the increased n_H may contribute to the observed reduction in μ_H. Wang *et al*. reported a μ_H which decreased as the amount of the Cu dopant increased,[33] while Zhou *et al*. saw a large decrease in μ_H and a shift to ionised impurity scattering at temperatures between 300−400 K.[34] Indeed, logarithmic plots of both mobilities against temperature (Figure S16) show ionised impurity scattering to be the dominant scattering mechanism across the measured temperature range, which is likely a result of the presence of the homogeneously distributed Cu^+ ions. The upshot being a mobility which increases approximately proportional to $T^{1.5}$, as the contribution from carrier-phonon scattering remains negligible.

Comparison of Hall mobility and weighted mobility in $SnSe_2$:Cu

To resolve the disagreement between μ_H and μ_W we considered the relationship between the two as well as the band structure of $SnSe_2$. The relationship is sometimes quoted as being $\mu_W \propto \mu_H(m^*/m_e)^{3/2}$ where m^* is the density of states (DOS) effective mass, and m_e is the electron rest mass,[43] although drift mobility is sometimes quoted in place of μ_H. Pisarenko plots were constructed to estimate m^* for both $SnSe_2$:Cu and bulk $SnSe_2$ at 350 K (Figure S17). The obtained m^* for bulk $SnSe_2$ were $1.0m_e$ (IP) and $1.2m_e$ (OOP), while $SnSe_2$:Cu had lower values of $0.4m_e$ (IP) and $0.6m_e$ (OOP). However, calculating μ_W using the measured μ_H and m^* does not account for the significant disagreement between the two measures of mobility. The answer comes from

electronic band structure calculations by Ding *et al*.[50] and others[51-53] who showed that $SnSe_2$ has two conduction band minima (CBM), at the *L* and Γ points. Furthermore, Ding *et al*. demonstrated that at lower carrier concentrations ($n \approx 10^{18}$ cm^{-3}), conduction occurs at the *L* point CBM, but once n reaches approximately 10^{19} cm^{-3}, the Fermi energy increases allowing conduction to also occur in the Γ point CBM. This means that as *n* increases, there is a shift away from single band conduction and the two divergent CBM both contribute to conduction. The Hall mobility, μ_H, depends on the assumptions of the single parabolic band (SPB) model and is inversely proportional to *n*, whereas weighted mobility, μ_W, is relatively independent of n and is known to be able to represent materials with more complex band structures,[43] thus the two differ when the SPB model no longer applies. This is clear in the mobility of bulk $SnSe_2$ (Figure 3h,i), where μ_W and μ_H closely agree until the temperature reaches approximately 470 K, above which the values diverge as n_H increases from 3.4 to 5.3 × 10^{18} cm^{-3} at 520 K. After this point, μ_H continues to decrease as n_H increases, due to the fact that it is inversely proportional to carrier concentration. This n_H value falls in the range suggested by Ding *et al*. for the transition point between conduction in the *L* and Γ point CBMs. In $SnSe_2$:Cu, the value of n_H throughout the measured temperature range lies above this value, suggesting that conduction should be occurring in both CBMs, and thus μ_W is likely to be the more reliable measure of mobility.

Returning to the question of effective mass, we can see that the calculated values of m^* in our $SnSe_2$:Cu samples are notably lower than those of the bulk $SnSe_2$. Ding *et al*. calculated that the Γ point CBM has a significantly lower m^* than the *L* point with values of $0.3038m_e$ for (L-H) and $0.083m_e$ for (Γ-M). Given that both CBM are active in the high carrier concentration $SnSe_2$:Cu, this could explain the observed lower effective mass of the whole sample. It is important to note that the two CBM in this case remain separate and that no band convergence is observed. This is

in contrast to other reports of band structure engineering in TE materials, which aim to cause band convergence as a way to increase m^* and thus S.[54,55] In fact, it is more analogous to reports of band divergence causing a reduction in m^*.[28] We can therefore say that the reduced effective mass lends weight to the idea that the increase in carrier concentration causes a shift from conduction in a single band, to conduction across the two divergent CBM at the L and Γ points.

Overall, we can conclude that, as a result of Cu doping, the increase in carrier concentration causes conduction across two divergent CBM, reducing the value of m^*. The effect of this reduction is to increase the mobility, despite the increase in grain boundaries and carrier concentration, as can be seen in the value of μ_W. Additionally, the presence of Cu^+ ions caused a shift to an ionised impurity scattering dominated system, in which mobility increases with temperature. The result is that the higher values of n_H and μ_W contribute to a significantly increased σ in both directions, with the increase in μ_W particularly important as it can increase σ without having a detrimental effect on the value of S.

The mechanisms of Cu-doping in $SnSe_2$

We have seen that even a small amount of Cu in $SnSe_2$ can cause a significant increase in n_H, as well as a change in the conduction behaviour and scattering mechanism. To investigate in more detail the role which Cu^+ ions play we conducted XAFS measurements of $SnSe_2$:Cu NSs and comparable Cu-free $SnSe_2$ NSs, for which the characterisation by XRD TEM and XPS is shown in Figure S18. Sn and Se K-edge XANES and EXAFS measurements were conducted and, while the Se spectra showed no significant change between $SnSe_2$ and $SnSe_2$:Cu (Figure S19), the Sn spectra showed some interesting differences. The Sn K-edge XANES spectra (Figure 4a) and its 1st derivative (Figure 4b) show that the $SnSe_2$:Cu sample had a 0.39 eV lower edge jump energy than the $SnSe_2$ sample. Since it is well known that the K-edge energy of Sn shifts to higher photon

energies when the oxidation state increases,[56,57] this result suggests that $SnSe_2$:Cu contains a small amount of Sn^{2+} (possibly Sn^{3+}, although unlikely) in addition to Sn^{4+}. The reduction of Sn^{4+} ions may be an indication of the presence of Cu^+ ions in interstitial sites, as a reduction in the oxidation state of Sn^{4+} would then be required to maintain the charge neutrality of the lattice.

The k^3-weighted EXAFS oscillations and their Fourier transforms are shown in Figures 4c,d. In Figure 4d the two largest peaks represent the Sn-Se and Sn-Sn paths, respectively. Fitting of the oscillations by FEFF calculation showed no significant change in the Sn-Se bond length between $SnSe_2$ and $SnSe_2$:Cu. However, the Sn-Sn bond length had shrunk by 0.025 Å (from 3.844 to 3.819 Å) – a significant difference within the reported capabilities of EXAFS analysis.[58-60] Next, we looked at the increase in peak amplitude in $SnSe_2$:Cu compared to $SnSe_2$, particularly for the Sn-Se path. Since peak intensity is related to coordination number, the significant increase indicates a higher coordination number within the Sn-Se bond distance. This suggests the presence of Cu, which, as suggested by the DFT calculations of Zhou *et al*., is likely to intercalate between the layers of $SnSe_2$.[34] If Cu ions are intercalated between the layers, but within the Sn-Se bond distance of an Sn atom, Coulombic attraction will pull Se^{2-} anions to the Cu^+ cation in a direction perpendicular to the Sn-Se bond (Figure 5a). The neighbouring Sn atoms' positions may then shift towards the space vacated by Se (Figure 5b). This would explain the reduction in the Sn-Sn path length, but the insignificant change in the Sn-Se bond length.

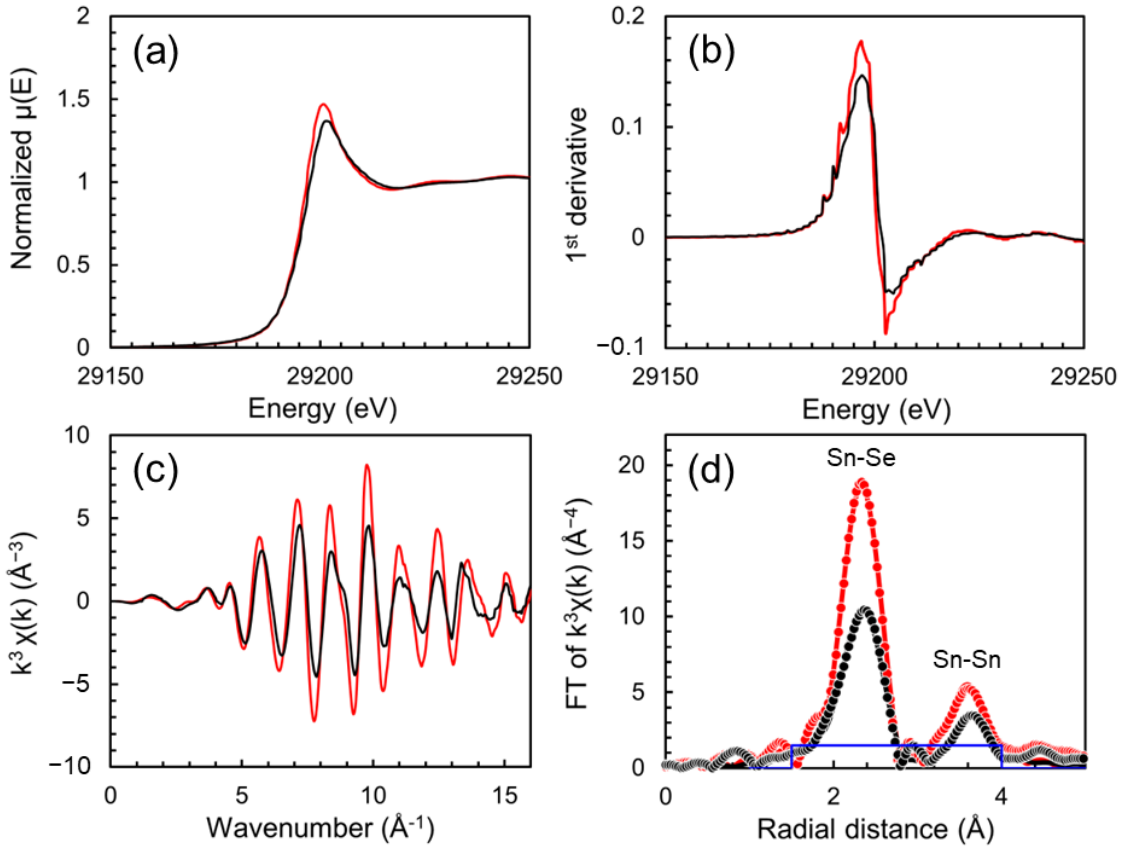

Figure 4. XAFS Sn K-edge spectra of $SnSe_2$ (black) and $SnSe_2$:Cu (red) NSs. (a) XANES, (b) 1st derivative of XANES, (c) k^3-weighted EXAFS oscillations, (d) Fourier transform (FT) of (c) (dotted lines) and FEFF calculation fittings (solid lines) for $SnSe_2$ and $SnSe_2$:Cu. The fitting window is indicated by the blue line.

To shed light on the effect of these intercalated Cu atoms on the electronic states of $SnSe_2$, a DFT calculation was performed using a simple 1×1×1 cell of $SnSe_2$ and a 2×2×2 supercell of $SnSe_2$:Cu, containing a single intercalated Cu atom. This does represent a slightly higher concentration of Cu than experimentally measured but was chosen to provide an insight into the potential effects while reducing the calculation time. The total density of states (DOS) for $SnSe_2$ and $SnSe_2$:Cu are shown in Figures 5c,d, respectively, and the partial DOS calculations are shown in Figure S20. We can see clearly in Figure 5d the contribution of the Cu orbitals to the valence

band of $SnSe_2$, which is mainly from the outer d orbital (Figure S20). The result is a significant shift in the Fermi level towards, and indeed into, the conduction band, indicating that n-type doping has taken place. Although the concentration is slightly higher than in our actual $SnSe_2$:Cu sample, we can clearly see that Cu^+ ions can cause significant electron doping, which is directly responsible for the observed increase in n_H in our $SnSe_2$:Cu sample.

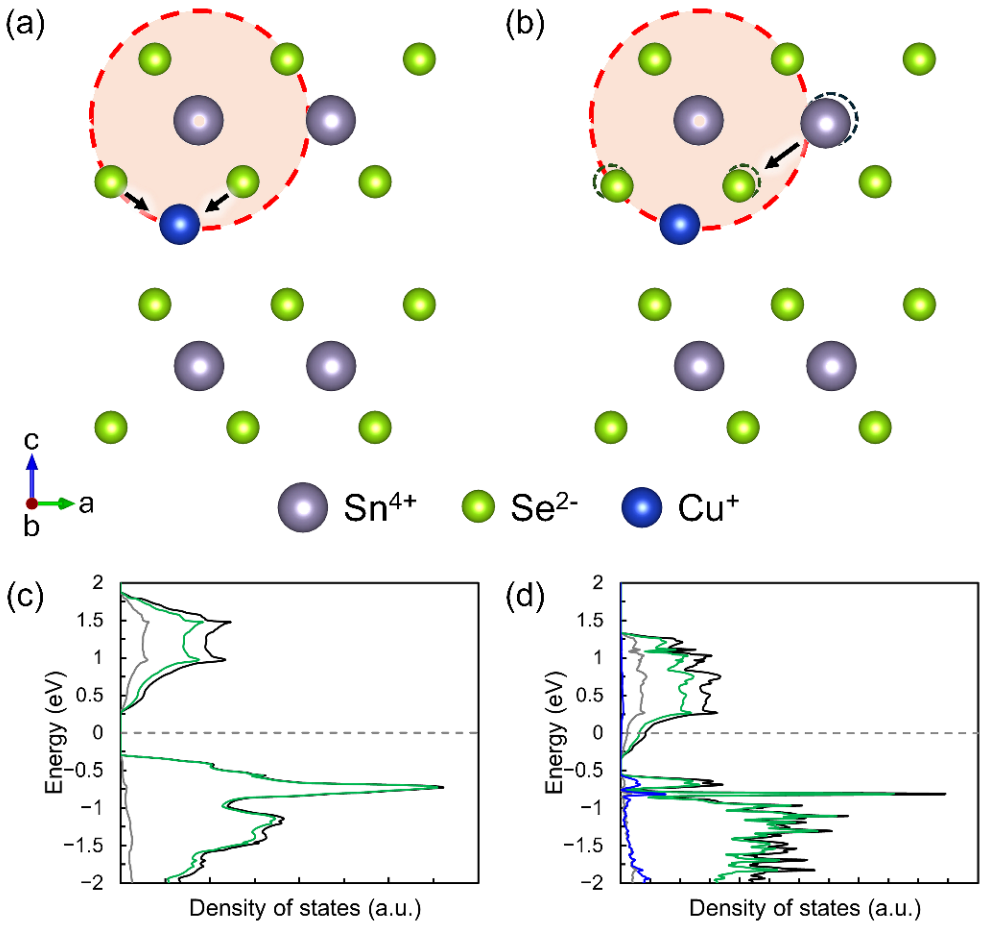

Figure 5. (a,b) Simple schematic image of Cu doping of $SnSe_2$. (a) Cu^+ ions intercalate in the VdW gap. Nearby Se atoms are attracted by Coulombic interaction in a direction perpendicular to the Sn-Se bond. (b) neighbouring Sn atom is drawn towards the vacated space, shortening the Sn-Sn distance. (c) DOS of a 1×1×1 cell of $SnSe_2$. (d) DOS of a 2×2×2 supercell of $SnSe_2$ containing one intercalated Cu atom. Black, grey, green, and blue represent total DOS and contributions from Sn, Se, and Cu, respectively. Fermi level (grey dashed line) is set at 0 eV.

CONCLUSIONS

By synthesising and sintering Cu doped $SnSe_2$ NSs we have produced $SnSe_2$:Cu pellets which have shown significantly higher TE properties than bulk, single crystal $SnSe_2$. This is down to both a reduced κ_l, due to phonon scattering at grain boundaries, and an increased σ, due to an increased n_{H} and μ_{W}. A maximum *ZT* of 0.6 at 667 K in the OOP direction demonstrates the potential of small amounts of Cu doping for practical, sustainable n-type TE materials, such as $SnSe_2$. The result also compares very favourably with other reports of Cu doping of $SnSe_2$, with only one report which included Br as a co-dopant and further heat treatment showing a higher TE performance. We then thoroughly investigated the mechanism of Cu doping and found that the Cu^+ ions are likely to have intercalated between the VdW layers, within the Sn-Se bond length. The presence of Cu^+ shifts the Fermi energy into the conduction band, leading to a significantly increased carrier concentration across the measured temperature range. This causes a change in the conduction mechanism from a single CBM to two divergent CBMs, thus reducing m^*. When combined with a shift to ionised impurity scattering under which mobility increases with temperature, the result is a significantly higher σ and *PF* across the measured temperature range. With the increased *ZT* value and mechanistic insight, we hope that this work will provide an important step towards practical, more sustainable TE materials.

ASSOCIATED CONTENT

The following files are available free of charge.

Experimental and DFT calculation details; schematic diagrams of the preparation process of the pellet for STEM and 3DAP analysis; pellet preparation for TE properties measurement; IP κ measurement using a thin pellet and COMSOL simulation; XRD and TEM analysis of the large-scale $SnSe_2$ NSs; STEM-EDS analysis of the $SnSe_2$:Cu NSs; XPS spectra of Cu 2p and Cu

$L_3M_{4,5}M_{4,5}$ Auger regions of the $SnSe_2$:Cu NSs; SEM-EDS and XPS composition results and XPS spectra of Cu 2p and Cu $L_3M_{4,5}M_{4,5}$ Auger regions of Sn (IV) acetate; TGA analysis of the $SnSe_2$:Cu NSs before and after the ligand exchange; STEM-EDS and SEM-EDS maps of the $SnSe_2$:Cu pellet; log-log plots of carrier mobility against temperature; Pisarenko plots; XRD, TEM, and XPS results of Cu-free $SnSe_2$ NSs; XAFS Se K-edge spectra; partial DOS calculations (PDF)

AUTHOR INFORMATION

Corresponding Author

***Shinya Maenosono** − School of Materials Science, Japan Advanced Institute of Science and Technology, 1-1 Asahidai, Nomi, Ishikawa 923-1292, Japan; E-mail: shinya@jaist.ac.jp

Authors

Simon Moore − School of Materials Science, Japan Advanced Institute of Science and Technology, 1-1 Asahidai, Nomi, Ishikawa 923-1292, Japan

Mari Takahashi − School of Materials Science, Japan Advanced Institute of Science and Technology, 1-1 Asahidai, Nomi, Ishikawa 923-1292, Japan

Philipp Sauerschnig − Global Zero Emission Research Center, National Institute of Advanced Industrial Science and Technology (AIST), Tsukuba, Ibaraki 305-8568, Japan

Keiji Kobayashi − School of Materials Science, Japan Advanced Institute of Science and Technology, 1-1 Asahidai, Nomi, Ishikawa 923-1292, Japan

Koichi Higashimine − Center for Nano Materials and Technology , Japan Advanced Institute of Science and Technology, 1-1 Asahidai, Nomi, Ishikawa 923-1292, Japan

Masanobu Miyata − School of Materials Science, Japan Advanced Institute of Science and Technology, 1-1 Asahidai, Nomi, Ishikawa 923-1292, Japan

Takahiro Baba − Research Center for Materials Nanoarchitectronics, National Institute for Materials Science (NIMS), 1-1 Namiki, Tsukuba, Ibaraki 305-0044, Japan

Jun Uzuhashi − Research Center for Magnetic and Spintronic Materials, National Institute for Materials Science (NIMS), 1-2-1 Sengen, Tsukuba, Ibaraki 305-0047, Japan

Michihiro Ohta − Global Zero Emission Research Center, National Institute of Advanced Industrial Science and Technology (AIST), Tsukuba, Ibaraki 305-8568, Japan

Takao Mori − Research Center for Materials Nanoarchitectronics, National Institute for Materials Science (NIMS), 1-1 Namiki, Tsukuba, Ibaraki 305-0044, Japan

Tadakatsu Ohkubo − Research Center for Magnetic and Spintronic Materials, National Institute for Materials Science (NIMS), 1-2-1 Sengen, Tsukuba, Ibaraki 305-0047, Japan

Author Contributions

The work was initiated by S.Ma. (Shinya Maenosono); S.Mo. (Simon Moore), M.T. and S.Ma. devised the method; S.Mo. constructed the experimental setup and performed all the experiments under the supervision of M.T. and S.Ma.; K.K. assisted in the experimental setup; K.H. conducted STEM observation of $SnSe_2$ nanosheets; P.S. measured thermoelectric properties of pellets under the supervision of M.O.; J.U. conducted STEM observation and 3DAP analysis of pellets under the supervision of T.O.; T.B. estimated the in-plane thermal conductivity of the $SnSe_2$:Cu pellet using the COMSOL simulation under the supervision of T.M.; S.Mo., M.T. and S.Ma. carried out XAFS measurements; M.M. performed the DFT calculation; S.Mo., M.T. and S.Ma. drafted the manuscript. All authors reviewed the manuscript and have given approval to the final version of the manuscript.

Funding Sources

This work was supported by JSPS KAKENHI (Grant Number 19H02440) and the Thermal and Electric Energy Technology Foundation. This work has also been partly supported by The

Research Grant against Global Warming of the Ichimura Foundation for New Technology. T.M. and T.B. thank JST Mirai JPMJMI19A1.

Notes

The authors declare no competing financial interest.

ACKNOWLEDGMENTS

This work was supported by JSPS KAKENHI under Grant No. 19H02440. This work was partially supported by the Thermal & Electric Energy Technology Foundation. T.M. and T.B. thank JST Mirai JPMJMI19A1. S. Mo thanks Fukue Kotegawa for her help with the XAFS measurements.

REFERENCES

[1] Fitriani; Ovik, R.; Long, B. D.; Barma, M. C.; Riaz, M.; Sabri, M. F. M.; Said, S. M.; Saidur, R. A Review on Nanostructures of High-Temperature Thermoelectric Materials for Waste Heat Recovery. *Renew. Sustain. Energy Rev.* **2016**, *64*, 635−659.

[2] Champier, D. Thermoelectric Generators: A Review of Applications. *Energy Convers. Manag.* **2017**, *140*, 167-181.

[3] Zoui, M. A.; Bentouba, S.; Stocholm, J. G.; Bourouis, M. A Review on Thermoelectric Generators: Progress and Applications. *Energies* **2020**, *13*, 3606.

[4] Palaporn, D.; Tanusilp, S. A.; Sun, Y.; Pinitsoontorn, S.; Kurosaki, K. Thermoelectric Materials for Space Explorations. *Mater. Adv.* **2024**, DOI: 10.1039/d4ma00309h.

[5] Mao, J.; Chen, G.; Ren, Z. Thermoelectric Cooling Materials. *Nat. Mater.* **2017**, *20*, 454-461.

[6] Shi, X. L.; Zou, J.; Chen, Z. G. Advanced Thermoelectric Design: From Materials and Structures to Devices. *Chem. Rev.* **2020**, *120*, 7399−7515.

[7] Yan, Q.; Kanatzidis, M. G. High-Performance Thermoelectrics and Challenges for Practical Devices. *Nat. Mater.* **2022**, *21*, 503−513.

[8] Chen, Y. X.; Zhang, J. Z.; Nisar, M.; Abbas, A.; Li, F.; Liang, G. X.; Fan, P.; Zheng, Z. H. Realizing High Thermoelectric Performance in n-type Bi_2Te_3 Based Thin Films *via* Post-Selenization Diffusion. *J. Materiomics* **2023**, *9*, 618-625.

[9] Lee, H.; Kim, T.; Son, S. C.; Kim, J.; Kim, D.; Lee, J.; Chung, I. Unique Microstructures and High Thermoelectric Performance in n-type $Bi_2Te_{2.7}Se_{0.3}$ by the Dual Incorporation of Cu and Y. *Mater. Today Phys.* **2023**, *31*, 100986.

[10] Jia, B.; Huang, Y.; Wang, Y.; Zhou, Y.; Zhao, X.; Ning, S.; Xu, X.; Lin, P.; Chen, Z.; Jiang, B.; He, J. Realizing High Thermoelectric Performance in Non-Nanostructured n-type PbTe. *Energy Environ. Sci.* **2022**, *15*, 1920-1929.

[11] Deng, R.; Su, X.; Zheng, Z.; Liu, W.; Yan, Y.; Zhang, Q.; Dravid, V. P.; Uher, C.; Kanatzidis, M. G.; Tang, X. Thermal conductivity in $Bi_{0.5}Sb_{1.5}Te_{3+x}$ and the Role of Dense Dislocation Arrays at Grain Boundaries. *Sci. Adv.* **2018**, *4*:eaar5606.

[12] Jai, B.; Wu, D.; Xie, L.; Wang, W.; Yu, T.; Li, S.; Wang, Y.; Xu, Y.; Jiang, B.; Chen, Z.; Weng, Y.; He, J. Pseudo-Nanostructure and Trapped-Hole Release Induce High Thermoelectric Performance in PbTe. *Science* **2024**, *384*, 81-86.

[13] Caballero-Calero, O.; Ares, J. R.; Martín-González, M. Environmentally Friendly Thermoelectric Materials: High Performance from Inorganic Components with Low Toxicity and Abundance in the Earth. *Adv. Sustain. Syst.* **2021**, *5*, 210095.

[14] Shen, Y.; Li, C.; Huang, R.; Tian, R.; Ye, Y.; Pan, L.; Koumoto, K.; Zhang, R.; Wan, C.; Wang, Y. Eco-Friendly P-Type Cu_2SnS_3 Thermoelectric Material: Crystal Structure and Transport Properties. *Sci. Rep.* **2016**, *6*, 32501.

[15] Wu, H.; Wang, G.; Peng, K.; Chi, H.; Zhang, B.; Chen, Y.; Li, C.; Yan, Y.; Guo, L.; Uher, C.; Zhou, X.; Han, X. Sodium-Doped Tin Sulfide Single Crystal: A Nontoxic Earth-Abundant Material with High Thermoelectric Performance. *Adv. Energy Mater.* **2018**, *8*, 1800087.

[16] Shi, Y.; Sturm, C.; Kleinke, H. Chalcogenides as Thermoelectric Materials. *J. Solid State Chem.* **2019**, *270*, 273−279.

[17] Li, F.; Zheng, Z.; Li, Y.; Wang, W.; Li, J. F.; Li, B.; Zhong, A.; Luo, J.; Fan, P. Ag-Doped $SnSe_2$ as A Promising Mid-Temperature Thermoelectric Material. *J. Mater. Sci.* **2017**, *52*, 10506−10515.

[18] Duong, A. T.; Nguyen, V. Q.; Duvjir, G.; Duong, V. T.; Kwon, S.; Song, J. Y.; Lee, J. K.; Lee, J. E.; Park, S. D.; Min, T.; Lee, J.; Kim, J.; Cho, S. Achieving *ZT*=2.2 with Bi-Doped N-Type SnSe Single Crystals. *Nat. Commun.* **2016**, *7*, 13713.

[19] Hong, M.; Chen, Z. G.; Yang, L.; Chasapis, T. C.; Kang, S. D.; Zou, Y.; Auchterlonie, G. J.; Kanatzidis, M. G.; Snyder, G. J.; Zou, J. Enhancing the Thermoelectric Performance of $SnSe_{1-x}Te_x$ Nanoplates Through Band Engineering. *J. Mater. Chem. A* **2017**, *5*, 10713.

[20] Pei, Y.; Wang, H.; Snyder, G. J. Band Engineering of Thermoelectric Materials. *Adv. Mater.* **2012**, *24*, 6125−6135.

[21] Biswas, K.; He, J.; Blu, I. D.; Wu, C. I.; Hogan, T. P.; Seidman, D. N.; Dravid, V. P.; Kanatzidis, M. G. High-Performance, Bulk Thermoelectrics with All-Scale Hierarchical Architectures. *Nature* **2012**, *489*, 414−418.

[22] Ortega, S.; Ibanez, M.; Liu, Y.; Zhang, Y.; Kovalenko, M. V.; Cadavid, D.; Cabot, A. Bottom-Up Engineering of Thermoelectric Nanomaterials and Devices from Solution-Processed Nanoparticle Building Blocks. *Chem. Soc. Rev.* **2017**, *46*, 3510−3528.

[23] Zhao, L. D.; Lo, S. H.; Zhang, Y.; Sun, H.; Tan, G.; Uher, G.; Wolverton, C.; Dravid, V. P.; Kanatzidis, M. G. Ultralow Thermal Conductivity and High Thermoelectric Figure of Merit in SnSe Crystals. *Nature* **2014**, *508*, 373−377.

[24] Kim, T.; Lee, H.; Chung, I. SnSe: The Rise of the Ultrahigh Thermoelectric Performance Material. *Bull. Korean Chem. Soc.* **2024**, *45* (3), 186-199.

[25] Chandra, S.; Biswas, K. Realization of High Thermoelectric Figure of Merit in Solution Synthesized 2D SnSe Nanoplates via Ge Alloying. *J. Am. Chem. Soc.* **2019**, *141*, 6141-6145.

[26] Zhou, C.; Lee, Y. K.; Yu, Y.; Byun, S.; Luo, Z. Z.; Lee, H.; Ge, B.; Lee, Y. L.; Chen, X.; Lee, J. Y.; Cojocaru-Miredin, O.; Chang, H.; Im, J.; Cho, S. P. Wuttig, M.; Dravid, P. V.; Kanatzidis, M. G.; Chung, I. Polycrystalline SnSe with a Thermoelectric Figure of Merit Greater than the Single Crystal. *Nat. Mater.* **2021**, *20*, 1387-1384.

[27] Chandra, S.; Bhat, U.; Dutta, P.; Bhardwaj, A.; Datta, R.; Biswas, K. Modular Nanostructures Facilitate Low Thermal Conductivity and Ultra-High Thermoelectric Performance in n-type SnSe. *Adv. Mater.* **2022**, *34*, 2203725.

[28] Chang, C.; Wu, M.; He, D.; Pei, Y.; Wu, C. F.; Wu, X.; Yu, H.; Zhu, F.; Wang, K.; Chen, Y.; Huang, L.; Li, J. F.; He, J.; Zhao, L D. 3D Charge and 2D Phonon Transports Leading to High Out-of-plane *ZT* in n-type SnSe Crystals. *Science* **2018**, *360*, 778-783.

[29] Byun, S.; Ge, B.; Song, H.; Cho, S. P.; Hong, M. S.; Im, J.; In C. Simultaneously Engineering Electronic and Phonon Band Structures for High-Performance n-type Polycrystalline SnSe. *Joule* **2024**, *8* (5), 1520-1538.

[30] Pham, A. T.; Vu, T. H.; Cheng, C.; Trinh, T. L.; Lee, J. E.; Ryu, H.; Hwang, C.; Mo, S. K.; Kim, J.; Zhao, L. D.; Duong, A. T.; Cho, S. High-Quality $SnSe_2$ Single Crystals: Electronic and Thermoelectric Properties. *ACS Appl. Energy Mater.* **2020**, *3*, 10787−10792.

[31] Xu, P.; Fu, T.; Xin, J.; Liu, Y.; Ying, P.; Zhao, X.; Pan, H.; Zhu, T. Anisotropic Thermoelectric Properties of Layered Compound $SnSe_2$. *Sci. Bull.* **2017**, *62*, 1663−1668.

[32] Pham, A. T.; Vu, T. H.; Nguyen, Q. V.; Vu, M. T.; Park, J. H.; Park, S. D.; Cho, S. Br-Doped N-Type $SnSe_2$: Single-Crystal Growth and Thermoelectric Properties. *ACS Appl. Energy Mater.* **2012**, *4*, 2908−2913.

[33] Wang, J.; Jian, X.; Lou, S.; Li, G.; Zhou, S. Cu-Embedded $SnSe_2$ with A High Figure of Merit at Ecofriendly Temperature. *ACS Omega* **2020**, *5*, 12409−12414.

[34] Zhou, C.; Yu, Y.; Zhang, X.; Cheng, Y.; Xu, J.; Lee, Y. K.; Yoo, B.; Cojocaru-Miredin, O.; Liu, G.; Cho, S. P.; Wuttig, M.; Hyeon, T.; Chung, I. Cu Intercalation and Br Doping to

Thermoelectric $SnSe_2$ Lead to Ultrahigh Electron Mobility and Temperature-Independent Power Factor. *Adv. Funct. Mater.* **2020**, *30*, 1908405.

[35] Nisar, M.; Qin, W.; Zhang, J.; Zheng, Z.; Li, F.; Liang, G.; Fan, P.; Chen, Y. X. Synergistic Optimization of Thermoelectric Performance in $SnSe_2$ through Co-doping: Anionic Vacancy Formation and Band Engineering. *Mater. Lab* **2023**, *2*, 230023.

[36] Wei, Y.; Li, J.; Zhang, D.; Zhang, B.; Zhou, Z.; Han, G.; Wang, G.; Prestipino, C.; Lemoine, P.; Guilmeau, E.; Lu, X.; Zhou, X. Phase-dependent Microstructure Modification Leads to High Thermoelectric Performance in n-type Layered $SnSe_2$ *Acta Mater* **2024**, *263*, 119504.

[37] Singh, N. K.; Bathula, S.; Gahtori, B.; Tyagi, K.; Haranath, D.; Dhar, A. The Effect of Doping on Thermoelectric Performance of P-Type SnSe: Promising Thermoelectric Material. *J. Alloys Compd.* **2016**, *668*, 152−158.

[38] Zheng, Z. H.; Fan, P.; Luo, J. T.; Liang, G. X.; Liu, P. J.; Zhang, D. P. Enhanced Thermoelectric Properties of Cu Doped ZnSb Based Thin Films. *J. Alloys Compd.* **2016**, *668*, 8−12.

[39] An, J.; Han, M. K.; Kim, S. J. Synthesis of Heavily Cu-doped Bi_2Te_3 Nanoparticles and Their Thermoelectric Properties. *J. Solid State Chem.* **2019**, *270*, 407−412.

[40] Liu, W. S.; Zhang, Q.; Lan, Y.; Chen, S.; Yan, X.; Zhang, Q.; Wang, H.; Wang, D.; Chen, G.; Ren, Z. Thermoelectric Property Studies on Cu-doped N-Type $Cu_xBi_2Te_{2.7}Se_{0.3}$ Nanocomposites. *Adv. Energy Mater.* **2011**, *1*, 577−587.

[41] Moore, S.; Kobayashi, K.; Takahashi, M.; Higashimine, K.; Maenosono, S. Facile Phase-Selectable Chemical Synthesis of Tin Selenide Nanosheets Towards Nanostructured Materials for Energy-Related Applications. *J. Phys. Chem. C* **2023**, *127*, 12394−12403.

[42] Lee, S. W.; Park, O.; Kim. S. I. Enhanced Thermoelectric Transport Properties of N-Type $SnSe_2$ Polycrystalline Alloys by Te Doping. *Int. J. Energy Res.* **2023**, 2900242.

[43] Snyder, G. J.; Snyder, A. H.; Wood, M.; Gurunathan, R.; Snyder, B. H.; Niu, C. Weighted Mobility. *Adv. Mater.* **2020**, *32*, 2001537.

[44] Ozaki, T. Variationally Optimized Atomic Orbitals for Large-Scale Electronic Structures. *Phys. Rev. B* **2003**, *67*, 155108.

[45] Ozaki, T.; Kino, H. Efficient Projector Expansion for the *ab initio* LCAO Method. *Phys. Rev. B* **2005**, *72*, 045121.

[46] Perdew, J. P.; Burke, K.; Ernzerhof, M. Generalized Gradient Approximation Made Simple. *Phys. Rev. Lett.* **1996**, *77*, 3865-3868.

[47] Yazdani, S.; Pettes, M. T. Nanoscale Self-Assembly of Thermoelectric Materials: A Review of Chemistry-Based Approaches. *Nanotechnology* **2018**, *29*, 432001.

[48] Jaih, A.; Ong, S. P.; Hautier, G.; Chen, W.; Richards, W. D.; Dacek, S.; Cholia, S.; Gunter, D.; Skinner, D.; Ceder, G Commentary: The Materials Project: A Materials Genome Approach to Accelerating Materials Innovation. *APL Mater.* **2013**, *1*, 011002.

[49] Uzuhashi, J.; Chen, J.; Kumar, A.; Yi, W.; Ohkubo, T.; Tanaka, R.; Takashima, S.; Edo, M.; Sierakowski, K.; Bockowski, M.; Sakurai, H.; Kachi, T.; Sekiguchi, T.; Hono, K. Atomic-Scale Investigation of Implanted Mg in GaN Through Ultra-High-Pressure Annealing. *J. Appl. Phys.* **2022**, *131*, 185701.

[50] Ding, Y.; Xiao, B.; Tang, G.; Hong, J. Transport Properties and High Thermopower of $SnSe_2$: A Full Ab-Initio Investigation. *J. Phys. Chem. C* **2017**, *121*, 225−236.

[51] Fong, C. Y.; Cohen, M. L. Electronic Energy-Band Structure of SnS_2 and $SnSe_2$. *Phys. Rev. B* **1972**, *5*, 3095−3101.

[52] Xia, C.; An, J.; Wei, S.; Jia, Y.; Zhang, Q. Electronic Structures and Optical Properties of $SnSe_{2(1-x)}O_{2x}$ Alloys. *Comput. Mater. Sci.* **2014**, 95, 712-717.

[53] Lochocki, E. B.; Vishwanath, S.; Liu, Z.; Dobrowolska, M.; Furdyna, J.; Xing, H. G.; Shen, K. M. Electronic Structure of $SnSe_2$ films grown by molecular beam epitaxy. *Appl. Phys. Lett.* **2019**, 114, 091602.

[54] Shenoy, U. S.; Goutham, K. D.; Bhat, D. K. Resonance States and Hyperconvergence Induced by Tungsten Doping in SnTe: Multiband Transport Leading to a Propitious Thermoelectric Material. *J. Alloys Compd.* **2022**, *905*, 164146.

[55] Zhao, L. D.; Wu, H. J.; Hao, S. Q.; Wu, C. I.; Zhou, X. Y.; Biswas, K.; He, J. Q.; Hogan, T. P.; Uher, C.; Wolverton, C.; Dravid, V. P.; Kanatzidis, M. G. All-scale Hierarchical Thermoelectrics: MgTe in PbTe Facilitates Valence Band Convergence and Suppresses Bipolar Thermal Transport for High Performance. *Energy Environ. Sci.* **2013**, *6*, 3346.

[56] Lützenkirchen-Hecht, D.; Scotti, N.; Jacobs, H.; Frahm, R. XAFS Investigations of Tin Nitrides. *J. Synchotron Rad.* **2001**, *8*, 698−700.

[57] McKeown, D. A.; Buechele, A. C.; Gan, H.; Pegg, I. L. Tin Valence and Local Environments in Silicate Glasses as Determined from X-ray Absorption Spectroscopy. *J. Non-Cryst. Solids* **2008**, *354*, 3142−3151.

[58] Gainar, A.; Stevens, J. S.; Jaye, C.; Fischer, D. A.; Schroeder, S. L. M. NEXAFS Sensitivity to Bond Lengths in Complex Molecular Materials: A Study of Crystalline Saccharides. *J. Phys, Chem. B* **2015**, *119*, 14373−14381.

[59] Hennig, G.; Reich, T.; Funke, H.; Rossberg, A.; Rutsch, M.; Bernhard, G. EXAFS as a Tool for Bond-Length Determination in The Environment of Heavy Atoms. *J. Synchotron Rad.* **2001**, *8*, 695−697.

[60] Newville, M.; Kas, J. J.; Rehr, J. J. Improvements in Modeling EXAFS with Many-Pole Self-Energy and FEFF8.5. *J. Phys.: Conf. Ser.* **2009**, *190*, 012023.